Available online at www.sciencedirect.com
SCIENCE DIRECT®
New Astronomy 9 (2004) 611–628
New Astronomy
www.elsevier.com/locate/newast

Evolution of morphological features of CMEs deduced from catastrophe model of solar eruptions

J. Lin *, W. Soon

Harvard-Smithsonian Center for Astrophysics, Solar, Stellar and Planetary Division, 60 Garden Street, MS-50, Cambridge, MA 02138, USA

Received 6 January 2004; received in revised form 3 April 2004; accepted 5 April 2004
Available online 22 April 2004
Communicated by W.D. Cochran

Abstract

We describe the evolution of morphological features of the magnetic configuration of CME according to the catastrophe model developed previously. For the parameters chosen for the present work, roughly half of the total mass is nominally contained in the initial flux rope, while the remaining plasma is brought by magnetic reconnection from the corona into the current sheet and from there into the CME bubble. The physical attributes of the difference in the observable features between CME bubble and flare loop system were studied. We tentatively identified distinguishable evolutionary features like the outer shell, the expanding bubble and the flux rope with the leading edge, void and core of the 3-component CME structure. The role of magnetic reconnection is discussed as a possible mechanism for the heating of the prominence material during eruptions. Several aspects of this explanation that need improvement are outlined.

PACS: 96.60.Hv; 96.60.Rd; 96.60.Be; 96.60.Wh

Keywords: Sun: coronal mass ejections (CMEs); Sun: magnetic fields; Sun: filaments; Plasmas; MHD

1. Introduction

In a recent review, Priest and Forbes (2002) pointed out that the main challenge for the theories of solar eruptions is to understand two basic aspects of eruptions. The two aspects are the cause of eruption itself and the nature of the observable features which form and develop during its evolution. The observables include bright flare ribbons on the solar disk and bright flare loops in the corona. Accumulation of our knowledge on the physical processes of solar eruptions (Wang et al., 2003; Ko et al., 2003) like solar flares, eruptive prominences and coronal mass ejections (CMEs) leads us to further believing that the observable features of solar

* Corresponding author. Tel./fax: +1-617-495-7425.
E-mail addresses: jlin@cfa.harvard.edu (J. Lin), wsoon@cfa.harvard.edu (W. Soon).

1384-1076/$ - see front matter
doi:10.1016/j.newast.2004.04.004

eruptions should also include rapid ejections of a large amount of magnetized plasma into the outermost corona and interplanetary space as well as detectable correlations of one manifestation to others (Zhang et al., 2002; Zhou et al., 2003). The mass, speed and magnetic orientation of the ejecta are the quantities that determine the geo-effectiveness of a CME. Hence, there is tremendous practical interests (see e.g., Srivastava and Venkatakrishnan, 2002; Venkatakrishnan and Ravindra, 2003; Yurchyshyn et al., 2004) for a fuller understanding and quantification.

As one of several possible mechanisms for triggering eruptions, the catastrophic loss of equilibrium in a coronal magnetic configuration has been extensively studied for more than two decades (see e.g., a recent review by Lin et al., 2003) since it was initially proposed by Van Tend and Kuperus (1978) and Van Tend (1979). Results of these works suggest that an MHD catastrophe constitutes the basic triggering of the major eruption, and that the magnetic reconnection driven by the catastrophe helps the loss of mechanical equilibrium in the relevant magnetic system develop into a plausible eruption (Forbes and Isenberg, 1991; Isenberg et al., 1993; Forbes and Priest, 1995; Lin and Forbes, 2000; Forbes and Lin, 2000; Lin, 2002).

Fig. 1 shows the proposed configuration of a disrupted magnetic field in the corona: a current-carrying flux rope, which is usually used to model the prominence, is thrust upwards by the catastrophic loss of equilibrium, and the adjacent closed magnetic field is stretched so severely that the field effectively opens up and a current sheet forms in the wake of the flux rope producing a Kopp–Pneuman-type structure (Kopp and Pneuman, 1976). Although gravity of the prominence material may be quantitatively important for some aspects of solar eruptions (see Forbes, 2000; Low, 2001), it is not essential for the catastrophe behavior of a magnetic system with relatively strong magnetic field (see discussions of Isenberg et al., 1993; Lin et al., 2003; and Lin, 2004 for more details). So, consideration of gravity is usually relaxed in the catastrophe models.

In the standard two-ribbon flare models (see Švestka and Cliver, 1992 and Forbes and Acton, 1996), magnetic reconnection invoked by plasma instabilities inside the current sheet creates both flare ribbons on the solar disk and flare loops in the corona (see the lower segment of the top panel and the enlargement in the bottom panel of Fig. 1). In the newly developed CME models, magnetic reconnection also plays an essential role in helping the upper extension of the magnetic structures escape into the outermost corona and interplanetary space (Mikić and Linker, 1994; Antiochos et al., 1999; Lin and Forbes, 2000; Forbes and Lin, 2000; Lin, 2002; Linker et al., 2003).

In general, the focus of the above theoretical works is either on the energetics or on the dynamics of an eruptive process. Parameters investigated include the total energy that could be released, velocity and acceleration of CME, evolution of the current sheet, the induced electric field inside the current sheet that may be responsible for various particle accelerations during the eruption, and so on. Generic scenarios of magnetic reconnection process suggest that reconnection outflow brings the reconnected plasma and magnetic flux leaving the reconnection site via both ends of the current sheet. As sketched by the cartoon in Fig. 1, magnetic reconnection is thus a prime driver for morphological changes in observable features of CMEs. So, as an extension of previous works, we are investigating here the impact of magnetic reconnection on the morphological features of an eruption, including the classical 3-component structure (i.e., the leading edge, void, and core) of some CME ejecta (Hundhausen et al., 1994; Low, 2001).

In Section 2, we quantitatively describe how the reconnected plasma is brought away from the corona during the eruptive process. In Section 3, we focus on the evolutionary and observable characteristics of the separatrix bubble – the area surrounded by the magnetic separatrix that is attached to the upper tip of the current sheet (see the thin red shell shown in the top panel of Fig. 1), as well as on the impact of the background field and the rate of magnetic reconnection on those features. In Section 4, strictly as a speculation, we qualitatively discuss the possible role played by reconnection in heating the prominence material during developmental stages of an impending

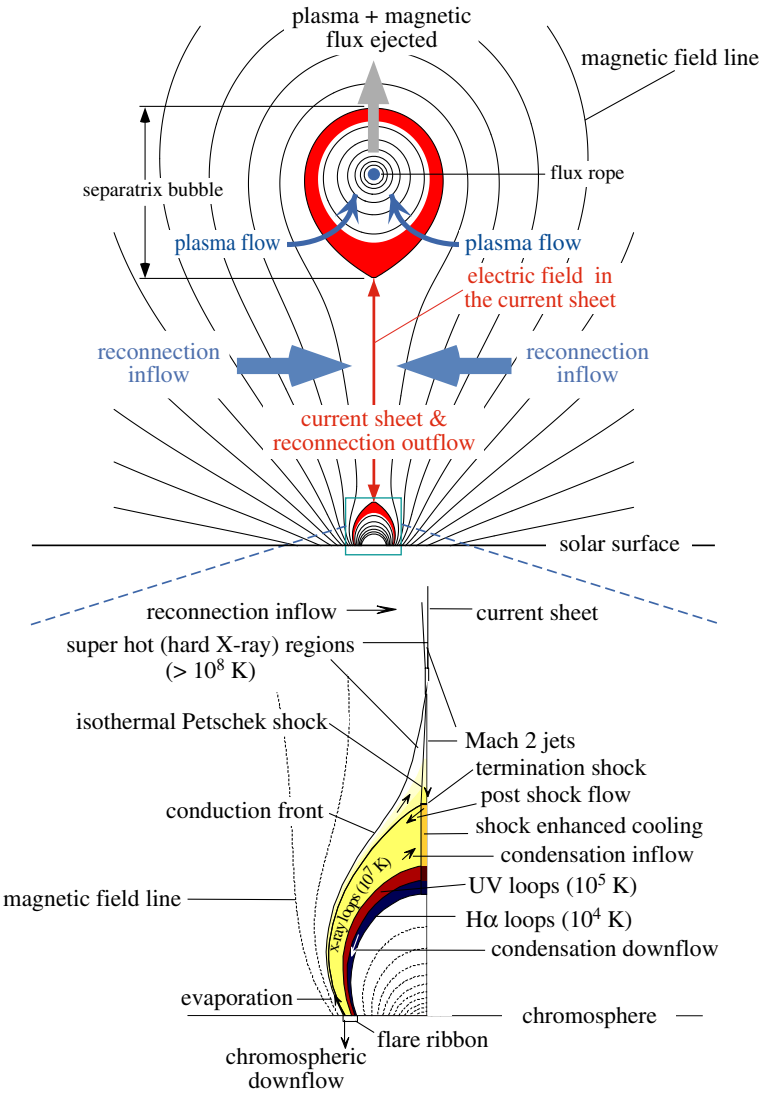

Fig. 1. Schematic diagram of a disrupted magnetic field that forms during an eruptive process. Colors are used to roughly denote the plasma layers in different temperatures. This diagram incorporates the two-ribbon flare configuration of Forbes and Acton (1996) and the CME configuration of Lin and Forbes (2000).

CME process. Finally, we summarize the work in Section 5.

2. Amount of plasma sent into space during eruption

Lin and Forbes (2000) constructed a model of solar eruptions. This model consists of a two-dimensional magnetic configuration in the semi-infinite x–y plane with $y = 0$ being the photospheric boundary (or more properly, the base of the corona) and $y > 0$ corresponding to the corona. At a given time, t, a force-free flux rope with radius r_0 is located at height h on the y-axis. Below it there may exist a detached vertical current sheet along the y-axis with its lower tip at $y = p$

and upper tip at $y = q$ as shown in Fig. 2. The background field in this configuration is produced by two point-source regions on the photosphere, which are separated by a distance of 2λ. The initial quasi-static evolution in the system in response to the slow decrease in λ eventually transits into a dynamic evolution due to the catastrophe occurring as λ reaches the critical value λ_c. The dynamic evolution of the catastrophic loss of equilibrium is rapid compared to the change in the background field. Therefore, λ can be considered unchanged after the catastrophe, and its value is thus fixed at λ_c in calculations of any parameter that describes the eruptive process.

On the basis of this model, we can calculate how much mass is sent into the bubble at any given time. As sketched in Fig. 1, the plasma that enters the bubble during the eruption has two sources. The first source is the reconnected plasma that is brought by the reconnection inflow (marked by the thick blue arrows in Fig. 1) from the corona near the current sheet and is then sent into the bubble through the current sheet by reconnection. This plasma is heated by reconnection as it passes through the current sheet. The other source is the direct plasma flow indicated by the blue curved arrows in Fig. 1. This plasma does not go through the current sheet before entering the bubble, but automatically becomes part of the bubble with the formation of new closed magnetic field lines, therefore it is not subject to heating in the current sheet.

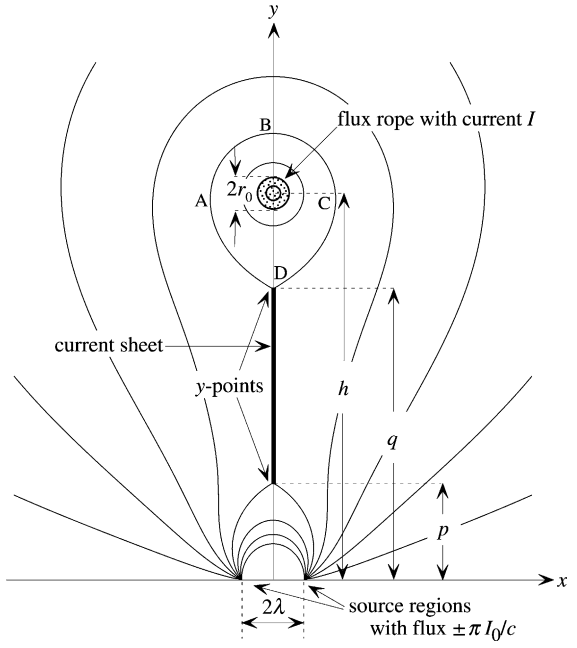

Fig. 2. Diagram of the CME/flux rope configuration that shows the mathematical notations used in the text (from Lin and Forbes, 2000). The height of the center of flux rope is denoted by h, while p and q denote the lower and the upper tips of the current sheet, respectively, the distance between the magnetic source regions on the photosphere is 2λ, and A, B, C, and D denote four specific points at the edge of the separatrix bubble such that the size of the bubble is measured either as ΔD, the span between A and C, or as Δh, the span between B and D.

For the plasma that goes through the current sheet, the inflow velocity of reconnection is $V_R = M_A V_A$, where M_A is the Alfvén Mach number and V_A is the local Alfvén velocity near the current sheet, so the total mass of plasma sent into the current sheet per unit time per unit length is (refer to Fig. 2)

$$\begin{aligned}\frac{dm}{dt} &= 2\int_p^q V_R(y)\rho(y)\,dy \\ &= 2M_A\int_p^q V_A(y)\rho(y)\,dy \\ &= 2M_A\rho_0\int_p^q V_A(y)f(y)\,dy, \end{aligned} \tag{1}$$

where the factor of 2 at the right-hand side is arising from the fact that the plasma flows from both sides into the current sheet, $\rho(y) = \rho_0 f(y)$ is the plasma mass density in the corona, ρ_0 is the value of $\rho(y)$ at the base of the corona, $f(y)$ is a dimensionless function that describes the variation of the mass density against height in the corona with $f(0) = 1$, and the integral is taken along the current sheet. The empirical function of the coronal plasma density deduced by Sittler and Guhathakurta (1999) is used in our calculations for $f(y)$, which reads as

$$\begin{aligned} f(y) = {} & a_1 z^2(y) e^{a_2 z(y)} \\ & \times [1 + a_3 z(y) + a_4 z^2(y) + a_5 z^3(y)], \end{aligned} \tag{2}$$

where

$$z(y) = 1/(1 + 5y/69.6), \quad a_1 = 0.001272,$$

$$a_2 = 4.8039, \quad a_3 = 0.29696,$$

$$a_4 = -7.1743, \quad a_5 = 12.321,$$

and y is in units of 5×10^4 km (see also Lin, 2002). Unlike the reconnected magnetic flux, the rates of reconnected plasma flowing from each end of the current sheet may not necessarily equal to one another. Because there is not a generally accepted theory about this rate, we assume, as a zeroth order approximation, that the reconnected plasma flows from each end of the current sheet at the same rate. So one half of the reconnected plasma enters the separatrix bubble.

On the other hand, it is not quite clear how to rigorously estimate the amount of mass for the plasma that does not go through the current sheet. We assume, for simplicity, that the amount of such plasma is the same as that of the reconnected plasma. So, the total mass injected into the bubble per unit time per unit length just equals $\mathrm{d}m/\mathrm{d}t$ given in (1). Since this non-current-sheet component of plasma comes from the region of higher altitudes where the plasma density is lower, we should keep in mind that taking the two plasmas to be equal to one another gives only an upper limit on the total mass inside the separatrix bubble. Our results deduced on the basis of (1) should be compared with the corresponding results of Lin (2002) in which neither of the above two added plasma masses were included in the propagation of CMEs.

The Alfvén velocity near the current sheet is given by:

$$V_{\mathrm{A}}(y) = \frac{B_y(0,y)}{\sqrt{4\pi\rho(y)}},$$

where $B_y(0,y)$ and $\rho(y)$ are the magnetic field and the plasma density measured just outside the current sheet, respectively (see Fig. 2 and the discussion in Lin and Forbes (2000) for further details). Applying the results of Lin and Forbes (2000) for the magnetic field and those of Lin (2002) for $\rho(y)$ we obtain

$$V_{\mathrm{A}}(y) = \frac{2I_0}{c\sqrt{4\pi\rho_0}} \times \frac{\lambda(h^2+\lambda^2)}{(h^2-y^2)(y^2+\lambda^2)} \sqrt{\frac{(q^2-y^2)(y^2-p^2)}{f(y)(p^2+\lambda^2)(q^2+\lambda^2)}},$$

where c is the light speed, I_0 is a constant with dimensions of electric current. Substituting $V_{\mathrm{A}}(y)$ into Eq. (1) yields

$$\frac{\mathrm{d}m}{\mathrm{d}t} = \frac{4I_0 M_{\mathrm{A}}\rho_0}{c\sqrt{4\pi\rho_0}} \times \int_p^q \frac{\lambda(h^2+\lambda^2)}{(h^2-y^2)(y^2+\lambda^2)} \sqrt{\frac{f(y)(q^2-y^2)(y^2-p^2)}{(p^2+\lambda^2)(q^2+\lambda^2)}}\,\mathrm{d}y, \tag{3}$$

which determines the rate of the reconnected plasma injected into the bubble, and parameters h, p, and q in Eq. (3) and other equations shown below are all functions of time, t, during the eruption. This component of plasma from reconnection may not enter the flux rope to modify the amount of mass inside the flux rope, but it does move with flux rope as it enters the bubble and affects the dynamical evolution of the flux rope.

Having an integral at the right-hand side of Eq. (3) makes it very difficult and time-consuming to solve the ordinary differential equations that govern the evolution of the system after the current sheet forms. To simplify calculations, we evaluate the integral approximately by multiplying the length of the current sheet with the integrand value at the middle of the current sheet. The basis of the approximation is the mean value theorem for definite integrals: the integral can be evaluated by taking product of the integral interval with the value of integrand at a given point within the interval. In our case, we assume this location to be the middle of the current sheet. (We will justify this approximation below.) Thus, Eq. (3) now becomes

$$\frac{\mathrm{d}m}{\mathrm{d}t} = \frac{4I_0 M_{\mathrm{A}}\rho_0}{c\sqrt{4\pi\rho_0}} \times \frac{\lambda(h^2+\lambda^2)(q-p)}{(h^2-y_0^2)(y_0^2+\lambda^2)} \sqrt{\frac{f(y_0)(q^2-y_0^2)(y_0^2-p^2)}{(p^2+\lambda^2)(q^2+\lambda^2)}}, \tag{4}$$

where $y_0 = (p+q)/2$.

The acceleration of the flux rope as well as the bubble, $\ddot{h}$, is related to the external force per unit length, F, acting on the flux rope, which is produced by the magnetic field from all the sources

(electric currents) outside the flux rope. F is given by

$$F = m\ddot{h},$$

where m is the total mass per unit length inside the bubble, which was previously fixed at $m_0 = 2.1 \times 10^6$ g cm^{-1} in the work of Lin and Forbes (2000) and Lin (2002), but is now free to vary with time, t, according to Eq. (4). From Lin and Forbes (2000), the force F is written as

$$F = \left(\frac{I_0}{c}\right)^2 \frac{\lambda^2}{2hL_{PQ}^2}\left[\frac{H_{PQ}^2}{2h^2} - \frac{(\lambda^2+p^2)(h^2-q^2)}{\lambda^2+h^2} - \frac{(\lambda^2+q^2)(h^2-p^2)}{\lambda^2+h^2}\right],$$

and we have (see also Eq. (36) of Lin and Forbes, 2000)

$$m\ddot{h} = m\dot{h}\dot{h}' = \left(\frac{I_0}{c}\right)^2 \frac{\lambda^2}{2hL_{PQ}^2}\left[\frac{H_{PQ}^2}{2h^2} - \frac{(\lambda^2+p^2)(h^2-q^2)}{\lambda^2+h^2} - \frac{(\lambda^2+q^2)(h^2-p^2)}{\lambda^2+h^2}\right], \quad (5)$$

where (and hereafter) the prime ($'$) means taking the derivative with respect to h, $L_{PQ}^2 = (\lambda^2+p^2)(\lambda^2+q^2)$, and $H_{PQ}^2 = (h^2-p^2)(h^2-q^2)$.

Other equations governing the flux rope motions given by Lin and Forbes (2000) remain valid and unchanged. These equations include the Faraday's equation that relates the change in the value of the flux function at the current sheet to the electric field, E_z, induced by the reconnection inflow near the current sheet, and the condition of frozen-in-flux at the surface of the flux rope. The Faraday's equation is written as

$$E_z = -\frac{1}{c}\frac{\partial A_0}{\partial t} = -\frac{1}{c}\frac{\partial A_0}{\partial h}\dot{h}, \quad (6)$$

where A_0 is the value of the flux function along the current sheet, and $\dot{h} = \mathrm{d}h/\mathrm{d}t$ is the flux rope velocity. The ideal-MHD environment outside the current sheet relates E_z to the velocity of reconnection inflow, V_R, and the magnetic field, $B_y(0,y)$, near the current sheet. To simplify our calculations below, we evaluate both the magnetic field and the Alfvén speed at the midpoint of the current sheet. This leads to

$$E_z = \frac{1}{c}V_R B_y(0,y_0) = \frac{1}{c}M_A V_A(y_0) B_y(0,y_0). \quad (7)$$

The combination of Eqs. (6) and (7) relates the dynamic properties of flux rope to the evolving reconnection process inside the current sheet and describes the quantitative dependence of the global evolutionary behavior of an eruption on the localized energy conversion occurring within a fairly confined area (more details concerning this relation can be found in Eqs. (24)–(28) as well as Eq. (40) of Lin and Forbes, 2000).

The condition of frozen-in-flux at the surface of the flux rope actually represents the ideal-MHD nature of the magnetic field and the plasma inside and outside the flux rope, it requires the flux function at the flux rope surface remain constant as the system evolves. In the work of Lin and Forbes (2000), this condition was expressed in both general and differential forms (refer to their Eqs. (30) and (32)). The general form is often used when we investigate the slow evolution of the system prior to the eruption and the differential form is used to close the differential equations (4)–(7) that govern the flux rope motions in the eruptive process.

To solve these sets of equations, the following characteristic values for various parameters in (4) and (5) are set for the purpose of normalization

$$\lambda_0 = 5 \times 10^4 \text{ km}, \quad m_0 = 2.1 \times 10^6 \text{ g/cm},$$

$$r_{00} = 0.1\lambda_0, \quad \rho_0 = 1.673 \times 10^{-14} \text{ g/cm}^3,$$

$$I_0/c\lambda_0 = 50\sigma \text{ G}, \quad \dot{h}_0 = 10^3 \text{ km/s},$$

where m_0 is the initial mass per unit length inside the flux rope, which is also used to normalize m, r_{00} is the initial value of the flux rope radius (Fig. 2), $I_0/c\lambda_0$ is one half the background field strength at the origin, σ in the expression for $I_0/c\lambda_0$ is a dimensionless constant describing the relative strength of the background field, and $\dot{h}_0$ is used to normalize velocity $\dot{h}$. The value of λ_0 adopted is appropriate for an eruption from an active region. Applying these values to Eq. (4), we have

$$\frac{\mathrm{d}m}{\mathrm{d}t} = 1.04204 M_{\mathrm{A}} \sigma \frac{\lambda(q-p)(h^2+\lambda^2)}{(h^2-y_0^2)(y_0^2+\lambda^2)} \times \sqrt{\frac{f(y_0)(q^2-y_0^2)(y_0^2-p^2)}{(p^2+\lambda^2)(q^2+\lambda^2)}}, \quad (8)$$

and applying them to Eq. (5) gives

$$\dot{h}\dot{h}' = \frac{3.125\lambda^2\sigma^2}{2.1mhL_{PQ}^2}\left[\frac{H_{PQ}^2}{2h^2} - \frac{(\lambda^2+p^2)(h^2-q^2)}{\lambda^2+h^2} - \frac{(\lambda^2+q^2)(h^2-p^2)}{\lambda^2+h^2}\right], \quad (9)$$

where the time, t, in Eq. (8), and hereafter, is in units of minutes. [1]

We are now ready to investigate the evolution of the system as a function of time. The governing equations consist of (8) and another four ordinary differential equations:

$$\frac{\mathrm{d}p}{\mathrm{d}t} = \frac{6}{5}p'\dot{h}, \quad \frac{\mathrm{d}q}{\mathrm{d}t} = \frac{6}{5}q'\dot{h},$$

$$\frac{\mathrm{d}\dot{h}}{\mathrm{d}t} = \frac{6}{5}\dot{h}'\dot{h}, \quad \frac{\mathrm{d}h}{\mathrm{d}t} = \frac{6}{5}\dot{h}, \quad (10)$$

which are the same as those in Eqs. (47) of Lin and Forbes (2000). Here, $\dot{h}\dot{h}'$ is given by (9), and the factor of 6/5 in Eq. (10) arises from the normalization of units. The expressions for p', q', and $\dot{h}'$ in (10) here were previously listed in Eq. (43) of Lin and Forbes (2000). To save space, we do not duplicate them.

In our calculations below, the rate of magnetic reconnection, M_{A}, is approximated by value measured at the center of the current sheet. In principle, M_{A} varies with time and the properties of the plasma and magnetic field near the reconnection site, such as the length and thickness of the current sheet, strength of the magnetic field and plasma resistivity. Since there is no generally accepted theory for how fast reconnection occurs when driven by a catastrophic loss of equilibrium, we assume that M_{A} is a constant less than unity in the present work. Consult works by Lin and Forbes (2000) and Forbes and Lin (2000) for detailed discussions of the functional behavior and the plausible values of M_{A}.

We next attempt to justify the use of magnetic reconnection rate measured at the midpoint of the current sheet to approximate the average rate of magnetic reconnection and the use of Eq. (4) to approximate equation (3). Fig. 3 gives the output power, P, of the eruptive process as a function of time for $\sigma = 1$ and $M_{\mathrm{A}} = 0.1$ which was derived from

$$P = m\dot{h}\frac{\mathrm{d}\dot{h}}{\mathrm{d}t}. \quad (11)$$

The solid curve corresponds to the case of evaluating the reconnection rate at the center of the current sheet, the dashed curve corresponds to the rate evaluated at the point with a distance of a quarter of $q-p$ from the lower tip of the current sheet, and the dotted-and-dashed curve to the rate at the point with the same distance from the upper tip of the current sheet. Fig. 3 confirms that the results for the three broad scenarios are not too different – for example, the difference between the solid curve and the average of the other two (da-

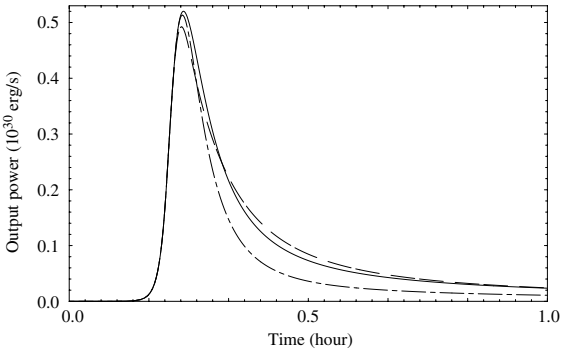

Fig. 3. Output powers of eruptive process corresponding to various locations where the rate of reconnection is evaluated along the current sheet. The results are used for justifying some approximations and modifications made in the present work. The solid curve corresponds to evaluating the reconnection rate at the center of the current sheet, the dashed curve corresponds to the rate at the center of the lower half section of the current sheet, and the dotted-and-dashed curve to the center of the upper half section.

[1] As in Lin and Forbes (2000), we ignore the force of gravity in our calculations for simplicity. The impact of gravity on CME propagation is small provided that the background field of the disrupted magnetic structure is not too weak, say not weaker than 30 G or $\sigma < 0.3$ (see Lin, 2004). In the present calculations, we take $\sigma \geqslant 0.5$.

shed and dot-dashed curves) is very small. Therefore, our approximation in evaluating the integrand in (3) at the middle of the current sheet is reasonable.

During the eruption, time $t = 0$ is set for the moment when the flux rope starts to lose its mechanical equilibrium. For the magnetic configuration we are dealing with, magnetic reconnection does not occur until $t = t^*$ when a neutral point appears at the boundary surface and a current sheet starts to develop (refer to Lin and Forbes, 2000 and Lin, 2002 for more discussions). So, the initial time for integrating Eqs. (4) and (10) is set at $t = t^*$. Thus, Eqs. (4) and (10) can be solved under the initial conditions (Lin and Forbes, 2000 and Lin, 2002)

$$\begin{aligned} &t = t^* = 12.213/\sigma, \quad h = h^* = 1.18113, \\ &\dot{h} = \dot{h}^* = 0.3211\sigma, \\ &m = m^* = 1, \quad p = p^* = 0, \quad q = q^* = 0. \end{aligned} \tag{12}$$

Fig. 4 shows the total mass of the reconnected plasma sent into the separatrix bubble against time (here we assume that the system extension in z-direction, L, is 10^5 km, see Lin and Forbes, 2000) for different background field strengths (Fig. 4(a)) and for different magnetic reconnection rates (Fig. 4(b)). Four curves in Fig. 4(a) from low to high correspond to $\sigma = 0.5$, 1, 2, and 3, respectively. The rate of magnetic reconnection in the relevant calculations is fixed at $M_A = 0.1$. These curves indicate that the amount of the reconnected plasma increases with the strength of the background field, and that most of the reconnected mass comes from the low corona. They also suggest that dependence of the added plasma on the strength of background field is not very significant. The curves in Fig. 4(b) are also for the variations of the added mass during the eruption, but the strength of the background field is fixed at $\sigma = 1$, and the rates of magnetic reconnection were evaluated with $M_A = 0.05$ (dashed curve) and $M_A = 0.1$ (solid curve), respectively. We note that the amount of the added plasma depends sensitively on the rate of magnetic reconnection. The increase in the mass of the added plasma with both the background field, σ, and the rate of magnetic reconnection, M_A, is because the velocity at which

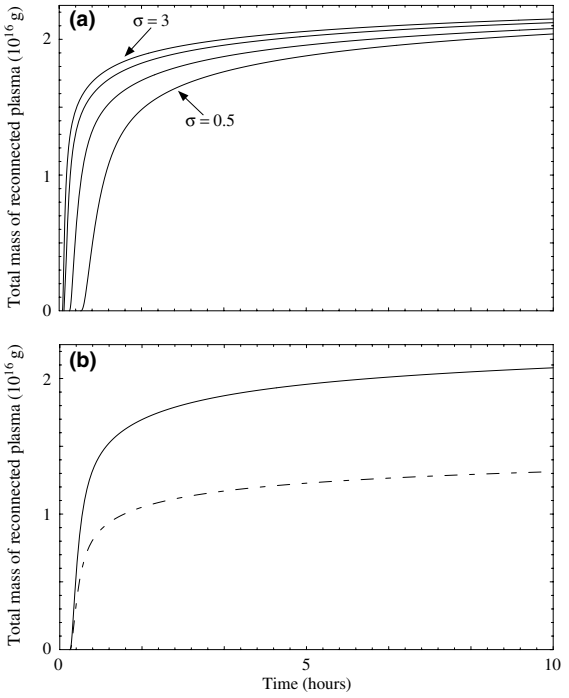

Fig. 4. Variations of the amount of reconnected plasma m versus time t for (a) fixed rate of magnetic reconnection with $M_A = 0.1$ and varying background fields: $\sigma = 0.5$, $\sigma = 1$, $\sigma = 2$, and $\sigma = 3$ from low to high (bottom to top curves), respectively, and for (b) fixed background field with $\sigma = 1$ and varying rates of magnetic reconnection: $M_A = 0.05$ (dashed curve) and $M_A = 0.1$ (solid curve), respectively.

the plasma is brought to the reconnection site is proportional to M_A and to the local Alfvén speed, which is also proportional to σ. The added material mostly originates in the low corona since the plasma is denser at lower altitudes. Comparison of the curves in Fig. 4(a) with those in Fig. 4(b) shows that the rate of magnetic reconnection is more important than the background field in determining the amount of the added plasma. This is owing to the fact that M_A governs the speed of plasma flowing into the reconnection site more directly than the background field.

Curves in Fig. 4 also imply that although most of the mass ($\sim 80\%$) from reconnection is added within the first 1–1.5 h after the onset of reconnection, the mass within the CME is continually increasing for a long duration of time. This dynamical reality means that average masses of

CMEs derived from the traditional coronagraph data near the Sun are underestimated. For example, the older coronagraph data gave a few times 10^{15} g for the masses carried away by CMEs (Howard et al., 1985; Hundhausen et al., 1994). But results from Helios (Webb et al., 1996) and LASCO (Howard et al., 1997) indicated that earlier mass estimates were underestimated by factors of 3–10, probably because mass outflow can persist well after the CME's leading edge has left the field of view of detectors (Webb, 2000). Most recently, Ko et al. (2003) analyzed a CME that leaves a long and thin streamer-like structure behind. The high ionization state of the plasma ([Fe XVIII] emission features were observed) inside this structure and a growing flare loop system in EIT 195Å right beneath it indicate that it is the current sheet that develops in a disrupted magnetic field, which is suggested by Lin and Forbes (2000). The continuous plasma outflow along the current sheet observed by Ko et al. (2003) seems to support Webb's (2000) conclusion and our theoretical result.

3. Observational implications of the evolution of separatrix bubble

As indicated by the cartoon in Fig. 1, the separatrix bubble that surrounds the flux rope and attaches to the upper tip of the current sheet is also the product of magnetic reconnection, like the post-flare/CME loop/giant arch system below the current sheet. During an eruption, coronal magnetic field and plasma are continuously reconnecting through the current sheet. The newly formed closed field lines, both of those anchored in the photosphere for flare loops and those surrounding the flux rope, are successively produced, causing both the flare loop system and the separatrix bubble to expand.

3.1. Morphological features

As shown by Fig. 2, the size of the bubble can be described either by ΔD, the span between points A and C, and/or by Δh, the span between points B and D. Because of the cusp structure near the tip of the current sheet, the scale of the bubble in y-direction, Δh, is slightly larger than that in x-direction, ΔD. By solving Eqs. (8) and (10), we are able to track the size of the magnetic system at any given time during the eruption. Fig. 5(a) shows ΔD and Δh versus time for $\sigma = 1$ and $M_A = 0.1$. Time $t = 0$ corresponds to the onset of the eruption. Before magnetic reconnection commences at $t = t^*$, the separatrix bubble does not show any distinctive changes from its original configuration that are observable. So the evolutions of ΔD and Δh at the stage prior to reconnection are represented with dashed curves. To demonstrate how the scale of the separatrix bubble varies with the propagation of the flux rope, we also plot h, $q + \Delta h$ (the height of the separatrix bubble apex, B, refer to Fig. 2), and q (the height of the separatrix bubble bottom, D) versus time in Fig. 5(b). These curves suggest that expansion of the separatrix bubble is fairly rapid during the eruption.

For the flux rope located at the center of the bubble, on the other hand, its scale and expansion are governed by internal force balance that is usually determined by the force-free condition inside the flux rope. The internal balance relates the flux rope radius, r_0, to the intensity of electric current, I, inside the flux rope. Parker (1974) derived an exact solution for force-free magnetic field in the flux rope. But the solution is implicit and transcendental, so it is cumbersome to use. Isenberg et al. (1993) simplified Parker's solution by fitting the $r_0 - I$ curve with a polynomial expression within the range of interests. When constructing CME models, we further simplify this relationship to

$$r_0 = r_{00}/J, \tag{13}$$

where $J = I/I_0$ and r_{00} is the value of r_0 for $J = 1$. A justification for using Eq. (13) to approximate the solutions of Parker (1974) and Isenberg et al. (1993) is given in Lin and Forbes (2000). Fig. 5(c) plots the time-profile of r_0 and Fig. 5(d) plots h and $h \pm r_0$, respectively, for the case of $M_A = 0.1$ and $\sigma = 1$. Comparing Figs. 5(c) and (d) with Figs. 5(a) and (b) indicates that the expansion of the flux rope itself is much slower than that of the

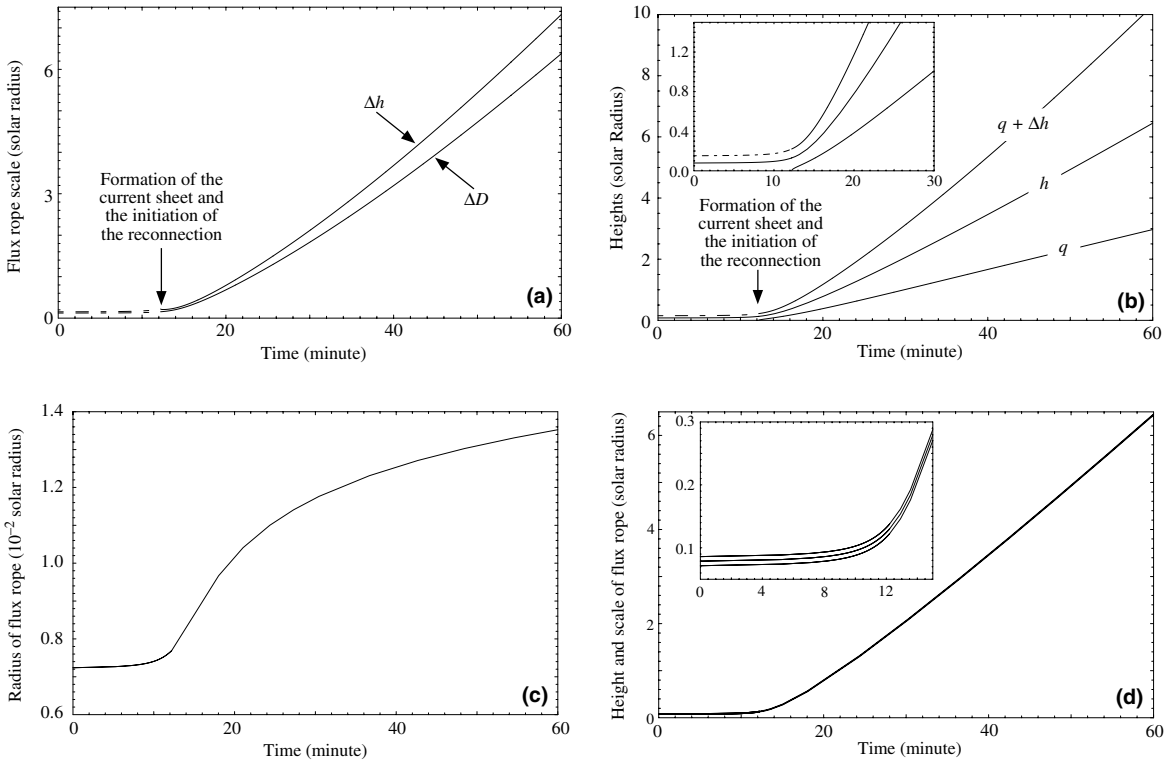

Fig. 5. Evolutions of the morphological features of the separatrix bubble and the scale of flux rope for $\sigma = 1$: (a) ΔD and Δh. (b) The parameters for morphological features of the separatrix bubble. The dashed section indicates the stage before reconnection starts. (c) The flux rope radius r_0. (d) The flux rope scale. The inset shows more details: the upper curve is for $h + r_0$, the lower curve is for $h - r_0$, and the middle one is for h.

separatrix bubble. This result suggests that the most rapidly expanding structure during CMEs is always the separatrix bubble instead of the flux rope (filament or prominence).

The snapshots in Fig. 6 capture the evolutions of various morphological features following the onset of the eruption ($M_A = 0.1$ and $\sigma = 1$). The starting configuration does not contain any magnetic reconnection site, such as X-type neutral point or current sheet, above the boundary surface as the catastrophe occurs at $t = 0$. So reconnection does not commence until $t = t^*$ when an X-type neutral point appears on the boundary surface and the current sheet starts to form. Magnetic reconnection continuously sends reconnected plasma and magnetic flux into the separatrix bubble through the upper tip of the current sheet which causes the volume of the bubble to increase rapidly (see Fig. 5(a)). Because of the freezing-in of plasma to magnetic field, the reconnected plasma and any associated thermal conduction flux can only be communicated through the separatrices. The closed field lines detached from the current sheet prevent the hot plasma from entering the interior segment of the separatrix bubble. Without a continuous supply of heat, the interior plasma starts to cool due to the adiabatic expansion and/or radiation. Therefore, the bubble's outer shell is hotter than its internal part and the colors in Fig. 6 are used to schematically denote this difference in temperature: red and yellow are for higher temperatures and green and blue are for lower ones. What happened to the flare loop system below the lower tip of the current sheet is similar: the hotter loops outside are enclosing the cooler ones inside.

Fig. 6 also indicates that the separatrix bubble above the current sheet grows much faster in both size and height than the corresponding flare loop

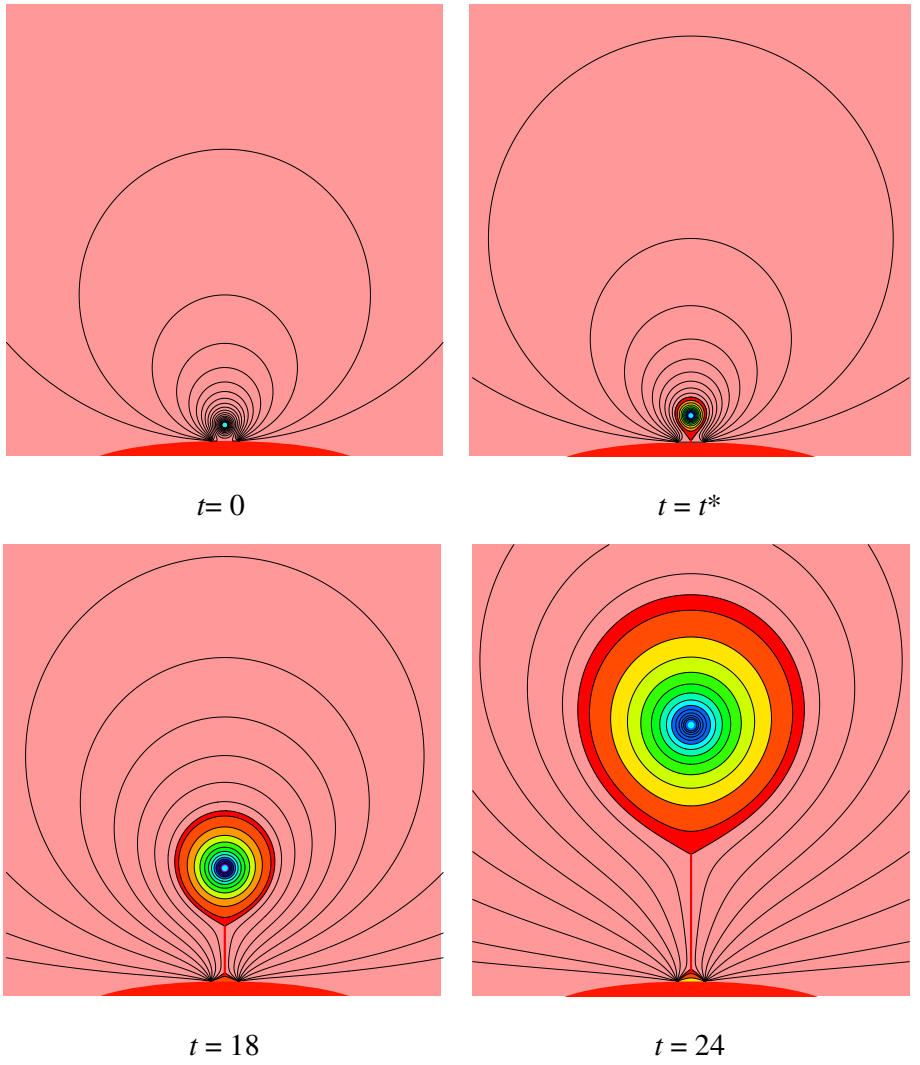

Fig. 6. Snapshots of the disrupted magnetic configuration at different times after the onset of the eruption. The eruption starts at $t = 0$, and magnetic reconnection does not commence until $t = t^*$ when a neutral point appears on the boundary surface and a current sheet begins to form.

system below the current sheet. This is because the flare loops occur in the lower corona with strong magnetic field and dense plasma compared to the upper corona in which the separatrix bubble propagates and expands. The tenuous plasma and weak magnetic field in the outermost corona and interplanetary space make it fairly easy for the separatrix bubble to grow. A detailed comparison of the curves in Figs. 5(a) and 5(b) with the solid curve in Fig. 6(g) of Lin (2002) provides us with a more quantitative understanding of the differences in sizes and in evolutionary behaviors between CMEs and flare loops. Interested readers may also refer to Švestka (1996), Lin (2002) and Ko et al. (2003) for more discussions and direct observational evidence.

3.2. Implications for 3-component structure of CMEs

Although our calculation is done in two-dimensions, the snapshots in Fig. 6 could be considered as cross-sections of a three-dimensional configuration, which includes a flux rope with two ends anchored in the photosphere (please see those three-dimensional configurations investigated numerically by Amari et al., 2003 and Linker et al., 2003). The evolutionary behavior of the disrupted magnetic field revealed by our snapshots in Fig. 6 still offers some valuable observational consequences. Because of the rapid growth of the bubble and the insufficient supply of plasma, the average density inside the bubble decreases quickly with time, and the bubble fades rapidly as it propagates through the outer corona and interplanetary space. However, fresh material is continually injected at the outer edge of the bubble, so a limb-brightened structure may be observable.

Two different densities of the plasma inside the separatrix bubble are plotted against the height of flux rope in Fig. 7 for a range of circumstances: (a) $\sigma = 0.5$ and $M_A = 0.05$, (b) $\sigma = 0.5$ and $M_A = 0.1$, (c) $\sigma = 1$ and $M_A = 0.05$, and (d) $\sigma = 1$ and $M_A = 0.1$. The dashed curves describe the plasma densities, $\bar{n}_1$, averaged over the volume surrounded by the separatrix S_1 (see Fig. 8), defined at the moment $t = t_1 = t^*$, when a neutral point just appears on the boundary surface and a current sheet starts to develop. The solid curves show the densities of the plasma, $\bar{n}_2$, averaged over the volume between S_1 and the instant (new) separatrix S_i at time $t = t_i > t^*$, where $i = 2, 3, \ldots$ (Fig. 8).

At time $t = t^*$, when magnetic reconnection begins in the reconnection site, the separatrix

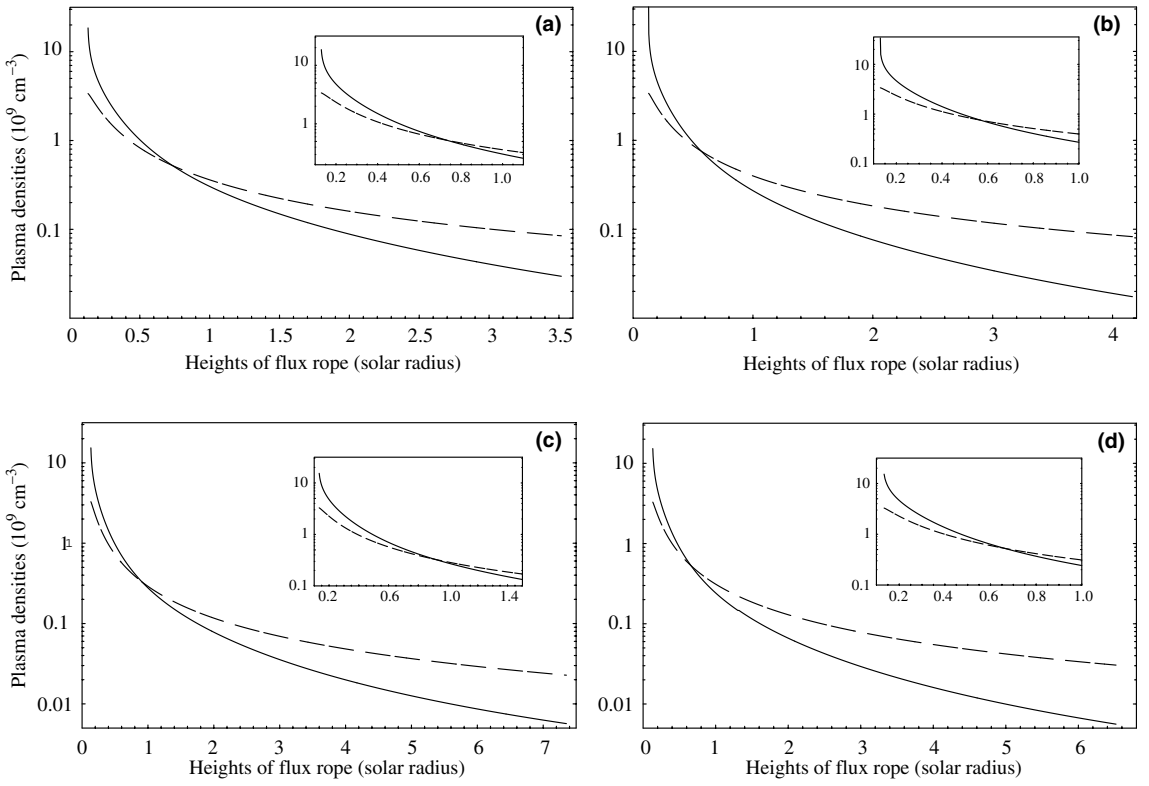

Fig. 7. Variations of the average densities of the plasma inside the separatrix bubble, $\bar{n}_1$ and $\bar{n}_2$, against the height of flux rope for (a) $\sigma = 0.5$, $M_A = 0.05$, (b) $\sigma = 0.5$, $M_A = 0.1$,(c) $\sigma = 1$, $M_A = 0.05$, and (d) $\sigma = 1$, $M_A = 0.1$. The dashed curves are for $\bar{n}_1$ and the solid curves for $\bar{n}_2$.

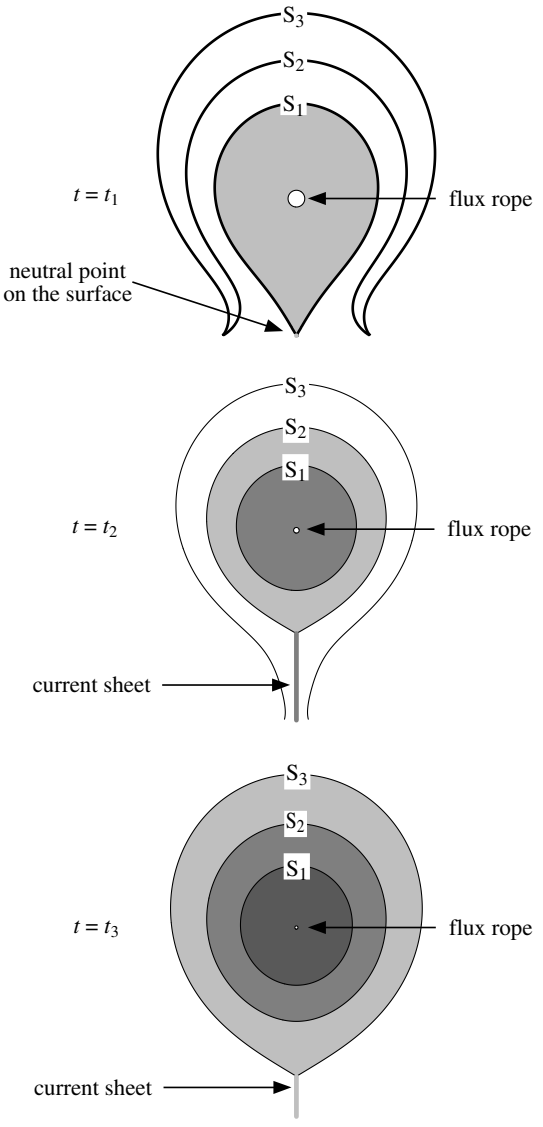

Fig. 8. Schematic descriptions of the evolution of the separatrix bubble in the eruptive process for (a) $t = t^* = t_1$, (b) $t = t_2$, and (c) $t = t_3$, respectively. To specify features of the separatrix, the three panels are not plotted on the same scale.

bubble surrounded by S_1 does not contain the plasma flowing from the reconnection site, but only that from pre-existing coronal background. As magnetic reconnection continues, S_1 detaches from the current sheet. Because of the freezing-in of plasma to magnetic field, the total amount of plasma inside S_1 does not therefore change. At time $t = t_2$, field line S_2 attaches to the current sheet and becomes the new separatrix. Progressive reconnection drives the separatrix from one field line S_1 to another one S_2, and then to another one, S_3, and so on (Fig. 8).

Fig. 8 also suggests that both densities, $\bar{n}_1$ and $\bar{n}_2$, will decrease quickly as the flux rope moves outward bringing the separatrix bubble together. Within a distance in radial direction of about five solar radii, density $\bar{n}_2$ decreases by more than two orders of the magnitude, and the decrease in $\bar{n}_1$ is also close to two orders of the magnitude. On the other hand, we also note that the corresponding curves in different panels in Fig. 7 show a similar pattern of characteristic decrease, which implies that the rate of magnetic reconnection and the background field do not significantly impact the variations of plasma densities inside the separatrix bubble. In short, the dependence of the average densities of plasma inside the separatrix bubble on the background field and on the rate of magnetic reconnection are totally different from the corresponding dependence of the added plasma mass inside the bubble.

In addition to the above dynamical evolution of CME morphological features, we find that the freezing-in of plasma to magnetic field also causes the plasma flowing out of the current sheet to be guided by the separatrix to fill a thin layer around the separatrix. The plasma density in this layer is a function of time, t, and altitude of flux rope, h. Fig. 9 shows the densities at three positions in this layer compared to the pre-CME densities at those heights for different σ and M_A (both were set to have the same values as in Fig. 7). As denoted in Fig. 2, position B is at the top of the bubble, C is at the edge of the bubble at the same height as the flux rope center, and D is at the upper tip of the current sheet. The solid curve corresponds to position B, the dashed curve to C and the dashed-and-dotted to D, respectively. Note that the density is assumed to be the same at all three locations in the bubble, but the density of the pre-CME corona varies by an order of magnitude at those heights according to Eq. (2). The behavior of each curve at its lower end may be owing to the fact that the amount of plasma injected into the bubble at low altitudes increases more slowly than the

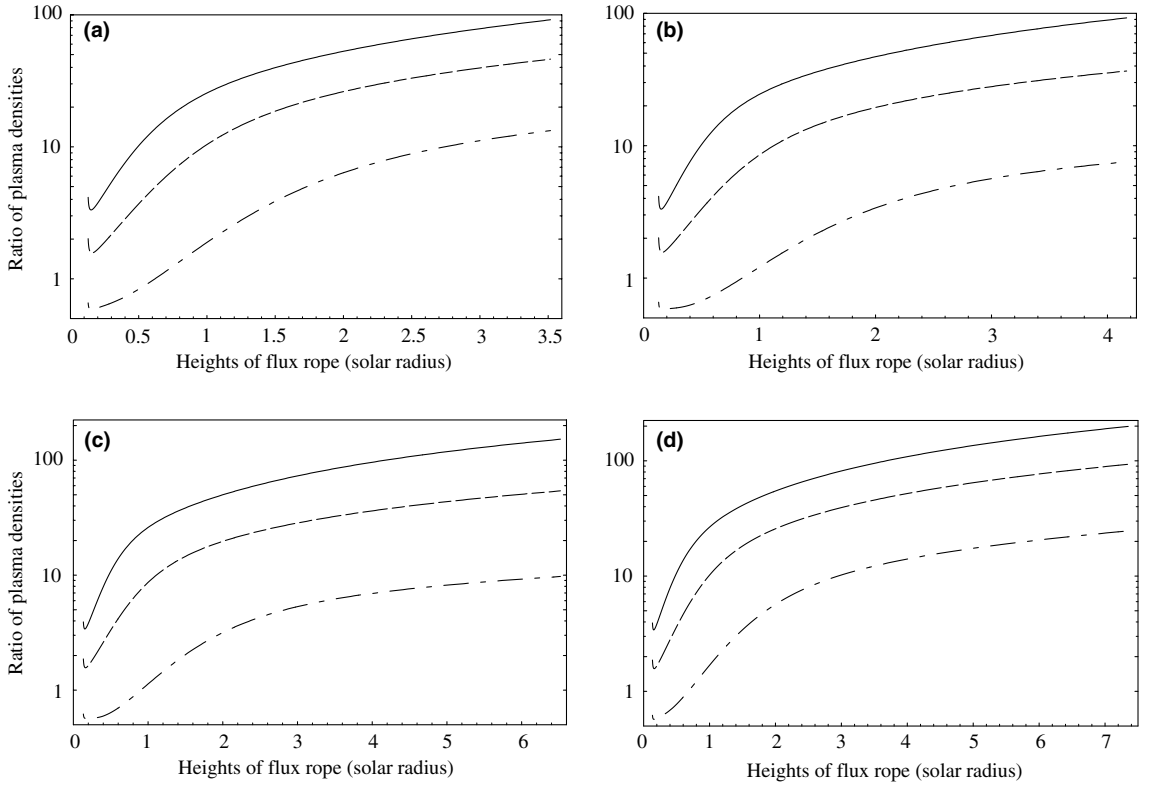

Fig. 9. Variations of the relative plasma densities in the outer shell of the separatrix bubble versus the corresponding altitude of flux rope, h, for (a) $\sigma = 0.5$, $M_A = 0.05$, (b) $\sigma = 0.5$, $M_A = 0.1$, (c) $\sigma = 1$, $M_A = 0.05$, and (d) $\sigma = 1$, $M_A = 0.1$, respectively. Solid curves are for density ratios measured at location B of the cartoon shown in Fig. 2, dashed curves for those at location C and dashed-and-dotted curves for location D.

volume of the bubble. Like $\bar{n}_1$ and $\bar{n}_2$ in Fig. 7, the density ratios specified in Fig. 9 depend weakly on both the background field and the rate of magnetic reconnection.

We can also show the density contrast between the dense shell around the separatrix and the bubble. Fig. 10 plots the densities of the plasma inside the shell compared to $\bar{n}_1$ and $\bar{n}_2$, respectively, for $\sigma = 1$ and $M_A = 0.1$. Those for different magnetic fields and different reconnection rates are not drawn since the impact of σ and M_A on the behaviors of the densities are weak like those revealed in Figs. 7 and 9. As mentioned previously, the plasma inside the shell is assumed to be uniform, so the results shown in Fig. 10 are independent of the positions where the density ratio is calculated.

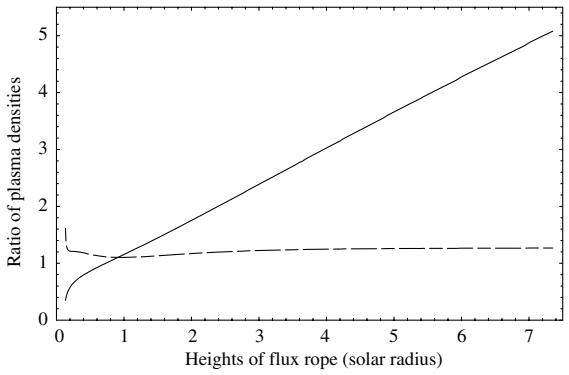

Fig. 10. Variations of the plasma densities in the dense shell compared to those in the bubble versus the corresponding altitude of flux rope, h, for $\sigma = 1$, $M_A = 0.1$, respectively. Dashed curve is for the density relative to $\bar{n}_1$, and solid curve for that relative to $\bar{n}_2$ (refer to Fig. 7).

The high and the medium density ratios indicated by Figs. 9 and 10, respectively, suggest that the dense shell at the outer edge of the bubble may correspond to the leading edge in the classic three-part structure of CMEs (Hundhausen et al., 1994; Low, 2001). It is possible that compressed plasma ahead of the bubble accounts for the bright leading edge, especially in CMEs that produce shocks. More detailed calculations will be needed to elucidate the relative contribution of compression ahead of the CME and plasma flow into the outer bubble from the current sheet. The CME bubble expands rapidly, so that the average density inside the bubble is lower than that within the outer shell of the bubble (Fig. 10). Thus the bubble can be naturally identified with the CME void from solar observations. Finally, the plasma inside the original flux rope, used to model the prominence in catastrophe model of CMEs, is initially in the range from 10^{11} to 10^{12} cm^{-3} (see Jensen et al., 1979; Tandberg-Hanssen, 1974; Priest, 1982) and this high-density material can be identified with the CME core.

Meanwhile, more detailed computations will be required to confirm the proposed identifications. In particular, we have simply assumed that plasma is injected into the outer shell of the bubble at a speed high enough that will be evenly distributed around the shell. A more modest injection speed would lead to a lower density at the CME front and a U-shaped or V-shaped structure at the top of the current sheet. U-shaped or V-shaped structures are observed in at least 10% of CMEs and are classified as Coronal Disconnection Events (Webb et al., 2003).

Before ending this section, we wish to point out that although the morphological features of CMEs manifested in above figures are deduced on the basis of the catastrophe model of solar eruptions developed by Lin and Forbes (2000), it does not necessarily mean that the catastrophe model is the only one that can replicate such features. Recent numerical simulations within the framework of the sheared arcade model of CMEs can also duplicate the disruptive magnetic configurations that we are studying in the present work. Fig. 11 borrows two illustrative snapshots from the three-dimensional simulations of Amari et al. (2003) and Linker et al. (2003). Similarities of the morphological features in these configurations to those shown in Fig. 6 are easily recognizable.

4. Speculations on the heating of CME ejecta

In addition to kinetic energy, much (perhaps as much as half) of the magnetic energy released in the eruption would be converted into thermal

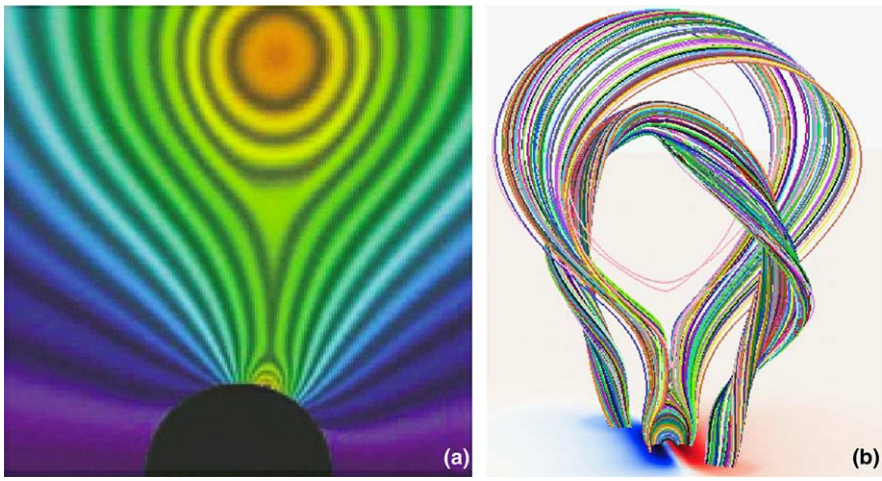

Fig. 11. Disrupted coronal magnetic fields produced in various numerical simulations: (a) from Linker et al. (2003) and (b) from Amari et al. (2003).

energy of plasma. So heating is another consequence of the CME models that include magnetic reconnection process but there is still no robust way to constrain how the magnetic energy dissipated by reconnection is divided between heating and kinetic energy. Recent works by Filippov and Koutchmy (2002), Ciaravella et al. (2000, 2001), Akmal et al. (2001) and Ji et al. (2003) suggest strong heating during eruptions.

By analyzing data from UVCS and LASCO instruments onboard the SOHO satellite, Ciaravella et al. (2000, 2001) studied the plasma density range and spatial structure of a CME observed on December 12, 1997. The analysis of elemental abundances indicates that the plasma ejected is chromospheric in origin and the spatial distribution of intensities of emission lines suggests that the bulk of ejected plasma may be entangled in an overall helical structure that consists of several separate strands. The UVCS spectroscopic diagnostics show that the ejecta emit over a wide range of temperatures from $10^{4.5}$ to $10^{5.5}$ K, and the cool kernel in C_{III} and other low temperature lines were surrounded by a warmer shell in O_V, O_{VI} and other high temperature lines. A composite image of C_{III}, O_V, and O_{VI} of a different CME on April 23, 1999 (Akmal et al., 2001) manifests the same structure of the ejecta. These two UVCS-LASCO works also indicate that the time interval in which the CME material remains emitting is much longer than the timescale of cooling due to radiation, adiabatic expansion, etc. Therefore, heat must be supplied somehow to balance the cooling.

The work by Filippov and Koutchmy (2002) shows a sudden change in the prominence material from absorption to emission in EUV at the beginning of an eruption. This CME event occurred on April 16, 2000. Unlike the eruption in the usual sense, the upward motion of the filament or prominence in this event stopped about half an hour after the onset. But it provides a unique chance for us to look carefully at how the prominence material changes associated with filament motion because in a typical eruption, the plasma and the magnetic flux quickly move away and one can hardly catch any details of the plasma and magnetic structure inside the prominence. The activity began with the slow rising of a dark filament (see Fig. 1 of Filippov and Koutchmy, 2002), then the filament was accelerated up to 100 km/s. Ten minutes after the onset and 6 min after the fast acceleration commences, some segments of the filament plasma became bright and emitting in EUV. Fine structures inside the filament indicate that the bright threads of plasma are entangled with the dark ones which implies that not all portions of the filament were heated during the eruption. The emission decayed shortly after the prominence stopped rising. A more recent work by Ji et al. (2003) shows a similar evolutionary behavior for a failed eruptive prominence: the eruption of prominence did not lead to a full-fledged CME. But hard X-ray emission near the top and the footpoints of the prominence, brightening of some original dark prominence material in EUV, as well as bright flare ribbons on the solar disk are significant features of this event.

Filippov and Koutchmy (2002) suggest that the magnetic energy is converted to the macroscopic kinetic energy of the filament motion and part of the kinetic energy of this motion is then turned into the heating of the plasma through particle collisions. According to their description, the collisions possibly takes place within many small shock fronts inside the flux rope.

From the point of view of heating by magnetic reconnection, we would consider magnetic reconnection as a plausible mechanism for heating the prominence material during the eruption. As demonstrated by the cartoon in Fig. 1 and the snapshots in Fig. 6, the hot reconnected plasma flowing out of the current sheet could be a good agent to heat the cold prominence material through mixing although in the configuration used in our calculations the hot and cold plasmas inside the bubble are strictly separated without being able to mix with one another (refer to stripes in different colors in Fig. 6). In reality, however, the magnetic field lines inside and around the flux rope may be highly or sufficiently tangled (see Amari et al., 2003 and Fig. 11(b)). So some internal reconnection occurring among the tangled field lines may cause the flux rope to evolve towards a simpler configuration, for example a linear force-free one. This is how, in principle, one could expect

both heating and some mixing of hot and cool plasma within and around the flux rope.

This scenario is not contrary to the theory of Filippov and Koutchmy (2002) since it is quite likely that those small shock fronts inside the prominence are results of internal magnetic reconnection. With this physical scenario, the prominence material is not only being heated directly but it is also allow to mix with the hotter plasma generated by magnetic reconnection in the current sheet below the flux rope (Figs. 1 and 6). Of course, more rigorous investigation will help clarify the physical mechanism and the amount of heating occurring during the eruptive process as well as whether the hot plasma injected to the separatrix bubble ought to appear in high temperature lines such as [Fe_{XVIII}] observed in some fast CMEs (Raymond et al., 2003).

5. Summary

As one of two basic aspects of solar eruptions, the morphological features of CMEs that form and evolve during the eruption are investigated in the present work on the basis of a catastrophe model of CMEs developed by Lin and Forbes (2000). The calculation indicates that around half of the magnetized plasma that is ejected into interplanetary space by CME is nominally contained in the initial flux rope, which is usually used to model the prominence under the framework of catastrophe model. The remaining plasma is brought from the corona in the vicinity of the current sheet by magnetic reconnection.

We suggest that the separatrix bubble, like the flare/CME loop/giant arch system, is the product of magnetic reconnection. As magnetic reconnection continues to send magnetized plasma into the separatrix bubble, the bubble swells very fast (i.e., much faster than flux rope). So, the "flux rope" that is often observed by coronagraphs may actually be a rapidly expanding separatrix bubble.

The analyses we conducted also suggest that the separatrix bubble possesses a thin outer shell that contains high temperature plasma that has just left the current sheet. This process probably causes the separatrix bubble to manifest the three-component feature of some CMEs. Comparison with observations indicate that further detailed studies of the three-component structure are needed.

We also noticed that a fraction of plasma that is heated by reconnection eventually leaves the reconnection site via the upper tip of the current sheet and is sealed in the separatrix bubble. Mixing of this part of plasma with cold prominence material may heat the latter causing it to change from absorption to emission in EUV. But this process depends on the complexity of the magnetic structure inside and around the prominence as well as on how the magnetic energy, dissipated by reconnection, is divided between heat and kinetic energy during eruptions. So more rigorous investigations are definitely necessary.

Acknowledgements

This work was supported by NASA under the Grants NAG5-12865 and NAG5-12827 to the Smithsonian Astrophysical Observatory, and by the Air Force Office of Scientific Research Grant AF49620-02-1-0194 to the Mount Wilson Institute. W.S. thanks Sallie Baliunas for collaborations and encouragement.

References

Akmal, A., Raymond, J.C., Vourlidas, A., Thompason, B., Ciaravella, A., Ko, Y.-K., Uzzo, M., Wu, R., 2001. ApJ 553, 922.

Amari, T., Luciani, J.F., Aly, J.J., Mikić, Z., Linker, J., 2003. ApJ 585, 1073.

Antiochos, S.K., DeVore, C.R., Klimchuk, J.A., 1999. ApJ 510, 485.

Ciaravella, A., Raymond, J.C., Thompson, B.J., van Ballegooijen, A., Strachan, L., Li, J., Gardner, L., O'Neal, R., Antonucci, E., Kohl, J., Noci, G., 2000. ApJ 529, 575.

Ciaravella, A., Raymond, J.C., Reale, F., Strachan, L., Peres, G., 2001. ApJ 557, 351.

Filippov, B., Koutchmy, S., 2002. SoPh 208, 283.

Forbes, T.G., 2000. J. Geophys. Res. 105 (A10), 23153.

Forbes, T.G., Acton, L.W., 1996. ApJ 459, 330.

Forbes, T.G., Isenberg, P.A., 1991. ApJ 373, 294.

Forbes, T.G., Lin, J., 2000. J. Atmos. Sol. Terr. Phys. 62, 1499.

Forbes, T.G., Priest, E.R., 1995. ApJ 446, 377.

Howard, R.A., Brueckner, G.E., St. Cyr, O.C., Biesecker, D.A., Dere, K.P., Koomen, M.J., Korendyke, C.M., Lamy, P.L.,

Llebaria, A., Bout, M.V., Michels, D.J., Moses, J.D., Paswaters, S.E., Plunkett, S.P., Schwenn, R., Sminett, G.M., Socker, D.G., Tappin, S.J., Wang, D., 1997. In: Crooker, N., Joselyn, J.A., Feynman, J. (Eds.), Coronal Mass Ejections. Amer. Geophys. Union, Washington, DC, p. 17.

Howard, R.A., Sheeley Jr., N.R., Michels, D.J., Koomen, M.J., 1985. J. Geophys. Res. 90 (A9), 8173.

Hundhausen, A.J., Stanger, A.L., Serbicki, S.A., 1994. Solar Dynamic Phenomena and Solar Wind Consequences. Noordwijk, ESTEC, The Netherlands. p. 409.

Isenberg, P.A., Forbes, T.G., Démoulin, P., 1993. ApJ 417, 368.

Jensen, E., Maltby, P., Orrall, F.Q. (Eds.), 1979. Physics of Solar Prominences. IAU Colloquium 44.

Ji, H., Wang, H., Schmahl, E.J., Moon, Y.-J., Jiang, Y., 2003. ApJ 595, L135.

Kopp, R.A., Pneuman, G.W., 1976. SoPh 50, 85.

Ko, Y., Raymond, J.C., Lin, J., Lawrence, G., Li, J., Fludra, A., 2003. ApJ 594, 1068.

Lin, J., 2002. ChJAA 2, 539.

Lin, J., 2004. SoPh 219, 169.

Lin, J., Forbes, T.G., 2000. J. Geophys. Res. 105, 2375.

Lin, J., Soon, W., Baliunas, S.L., 2003. NewAR 47, 53.

Linker, J.A., Mikić, Z., Lionello, R., Riley, P., 2003. Phys. Plasma 10 (5), 1971.

Low, B.C., 2001. J. Geophys. Res. 106, 25141.

Mikić, Z., Linker, J.A., 1994. ApJ 430, 898.

Parker, E.N., 1974. ApJ 191, 245.

Priest, E.R., 1982. Solar MHD. Reidel, Boston. pp. 127–129.

Priest, E.R., Forbes, T.G., 2002. A&ARv 10, 313.

Raymond, J.C., Ciaravella, A., Dobrzycka, D., Strachan, L., Ko, Y.-K., Uzzo, M.M., Raouafi, A.-E., 2003. ApJ 597, 1106.

Sittler, E.C., Guhathakurta, M., 1999. ApJ 523, 812.

Srivastava, N., Venkatakrishnan, P., 2002. Geophys. Res. Lett. 29 (9), 1287.

Švestka, Z., 1996. SoPh 169, 403.

Švestka, Z., Cliver, E.W., 1992. In: Švestka, Z., Jackson, B.V., Machado, M.E. (Eds.), Eruptive Solar Flares. Springer, New York, pp. 1–14.

Tandberg-Hanssen, E., 1974. Solar Prominences. Reidel, Dordrecht, Holland.

Van Tend, W., 1979. SoPh 61, 89.

Van Tend, W., Kuperus, M., 1978. SoPh 59, 115.

Venkatakrishnan, P., Ravindra, B., 2003. Geophys. Res. Lett. 30 (23), 2181.

Wang, H., Qiu, J., Jing, J., Zhang, H., 2003. ApJ 593, 564.

Webb, D.F., 2000. IEEE Trans. Plasma Sci. 28 (6), 1759.

Webb, D.F., Burkepile, J., Forbes, T.G., Riley, P., 2003. J. Geophys. Res. 108 (A12), 1440.

Webb, D.F., Howard, R.A., Jackson, B.V., 1996. In: Winterhalter, D. et al. (Eds.), Solar Wind Eight. American Institute of Physics, Woodburg, NY, p. 540.

Yurchyshyn, V., Wang, H., Abramenko, V., 2004. Space Weather 2, S02001, 10.1029/2003SW000020.

Zhang, M., Golub, L., DeLuca, E., Burkepile, J., 2002. ApJ 574, L97.

Zhou, G., Wang, J., Cao, Z., 2003. A&A 397, 1057.